Journal of
Microscopy

Journal of Microscopy, Vol. 260, Issue 2 2015, pp. 194–199 doi: 10.1111/jmi.12282
Received 27 February 2015; accepted 8 June 2015

A large-field polarisation-resolved laser scanning microscope: applications to CARS imaging

G. DE VITO*,†, A. CANTA‡, P. MARMIROLI‡ & V. PIAZZA*
**Center for Nanotechnology Innovation @NEST, Istituto Italiano di Tecnologia, I-56127, Pisa, Italy*
†NEST, Scuola Normale Superiore, I-56127, Pisa, Italy
‡Experimental Neurology Unit, Department of Surgery and Translational Medicine, University of Milan–Bicocca, Monza, Italy

Key words. Coherent Anti-Stokes Raman Scattering, large field-of-view, laser-scanning imaging, polarisation-resolved, RP-CARS.

Summary

Laser-scanning imaging techniques are frequently used to probe the molecule spatial orientation in a sample of interest by exploiting selection rules depending on the polarisation of the excitation light. For the successful implementation of these techniques the precise control of the polarisation at the sample level is of fundamental importance. Polarisation distortions induced by the optical elements are often the main limitation factor for the maximum size of the field-of-view in polarisation-resolved (PR) laser-scanning microscopy, since for large scanning angles the polarisation distortions may mask the real sample structure. Here we shall demonstrate the implementation of large-field-of-view PR microscopy and show PR CARS imaging of mouse spinal cord thanks to a careful design of the laser-beam optical path. We shall show that this design leads to strongly suppressed distortions and quantify their effects on the final images. Although the focus of this work is on CARS imaging, we stress that the approaches described here can be successfully applied to a wide range of PR laser-scanning techniques.

Introduction

PR laser-scanning microscopy is a term that encompasses a broad range of laser-scanning imaging techniques that share the ability to probe the sample properties by exploiting polarisation-dependent effects and different signal-generation processes, including single-photon (Finzi & Bustamante, 1988; Steinbach *et al.*, 2009; Kress *et al.*, 2013) and two-photon fluorescence (Gasecka *et al.*, 2009; Savoini *et al.*, 2012; Ferrand *et al.*, 2014), label-free, second-harmonic generation (Plotnikov *et al.*, 2006; Tiaho *et al.*, 2007; Gusachenko *et al.*, 2010; Duboisset *et al.*, 2012; Mazumder *et al.*, 2012), and sample absorption (Finzi & Bustamante, 1988; Gupta & Kornfield, 1994).

Recently, novel label-free polarisation-resolved laser-scanning techniques were also presented based on four-wave mixing imaging (Munhoz *et al.*, 2012; Bioud *et al.*, 2014) and Coherent Anti-Stokes Raman Scattering (CARS) imaging (Zimmerley *et al.*, 2010; de Vito *et al.*, 2012; Bioud *et al.*, 2014). The latter is a powerful and innovative technique that relies on the coherent build-up of Raman anti-Stokes signal from resonant coherently oscillating molecular dipoles (Maker & Terhune, 1965). This label-free imaging technique is based on chemical contrast, like traditional Raman microimaging, but the signal intensity is typically several orders of magnitude stronger than spontaneous Raman, therefore enabling rapid imaging with high signal-to-noise ratio (SNR). CARS is a four-wave mixing process in which the energy difference of a pair of incoming ('pump' and 'Stokes') photons matches the energy of one or more vibrational modes of the target molecules. These coherently excited vibration modes are then probed by a third photon ('probe') and relax to the ground state via the emission of a fourth photon (the CARS signal). Due to the process selection rules, if the target molecular bonds are oriented anisotropically inside the PSF volume, then the CARS signal intensity is dependent on the orientation of the incident beams polarisation planes. Recently, a new CARS technique was presented, called 'RP-CARS' (de Vito *et al.*, 2012), which actively exploits this polarisation-dependent effects in order to measure the in-plane anisotropy of the molecular bonds of interest. Briefly, in this technique the CARS signal originating from each raster-scan point is probed with different orientations of the linearly polarised pump-and-probe incident beam (while the Stokes beam is kept circularly polarised) and then the amplitude and the phase of the Fourier components of the CARS signal are retrieved (de Vito & Piazza, 2014). The amplitude ($A_{2\omega}$) of the Fourier component of the CARS signal at twice the rotation frequency of the polarisation plane is a measure of how much the raw CARS signal varies during a

Correspondence to: Vincenzo Piazza, Laboratorio NEST, Complesso San Silvestro, Piazza San Silvestro 12, 56127 Pisa, Italy. Tel: +39-050-509495; fax: +39-050-509417; e-mail: vincenzo.piazza@iit.it

rotation of the waveplate and consequently it quantifies the in-plane anisotropy of the resonant molecular bonds orientation inside the PSF volume. The phase value (Φ) indicates the average spatial orientation of the dipoles. This approach was successfully exploited in a recent paper (de Vito *et al.*, 2014) to determine in real time and in a label-free all-optical scheme the myelin health status in a chemical model of demyelination.

In all of the aforesaid scanning imaging techniques it is of crucial importance that the polarisation distortions induced by the optical elements, in particular dichroic mirrors (DMs), are made as small as possible, for example, by compensating them with a combination of λ/2 and λ/4 waveplates (Bélanger *et al.*, 2009) or by adding a matched dichroic to the optical path (Bélanger *et al.*, 2015). Distortions introduced by dichroics typically vary strongly when the light incidence angle is changed by the galvanometric mirrors during the raster scanning and it does not seem feasible to compensate those distortions simply by adjusting the retarders in real time during the image acquisition. This issue is often the main limiting factor for the field-of-view in polarisation-resolved laser-scanning microscopy. A postprocessing approach was also developed (Bioud *et al.*, 2014) to subtract the preliminarily characterised distortions for small scanning angles from the detected signal. In this paper we present an original optical arrangement that allows for large-field RP-CARS microscopy with highly reduced distortions over the entire field-of-view. We stress that our approach can be straightforwardly implemented also in other types of PR laser scanning microscopies.

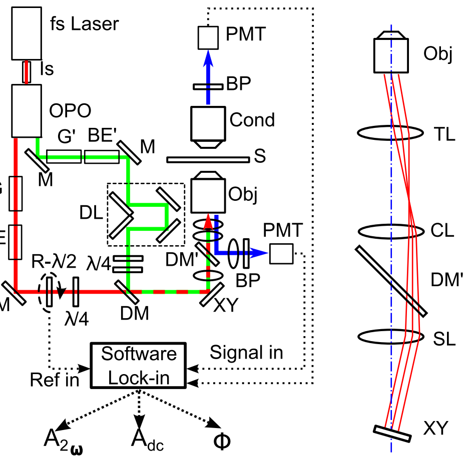

Fig. 1. Left: RP-CARS setup. Femtosecond laser (fs Laser), Faraday optical isolator (Is), optical parametric oscillator (OPO), SF6 optical glasses (G and G'), beam expander (BE), dichroic mirrors (DM, DM'), rotating half-wave plate (R-λ/2), quarter-wave plate (λ/4), delay line (DL), galvanometric mirrors (XY), sample (S), microscope objective (Obj), condenser (Cond), band-pass filter (BP), photomultipliers (PMT). The custom-made software (Software Lock-in) computes A_{dc}, $A_{2\omega}$ and Φ values from the detected signals. Thick red, green and blue lines show the paths of the pump, Stokes and signal beams respectively. Right: Detail of the laser-scanning optics, showing the scan lens (SL), the compensation lens (CL), the tube lens (TL, inside the microscopy body), the objective (Obj), and the galvanometric mirrors (XY). The blue dash-dotted line indicates the optical axis. The red lines indicate the beam path.

Materials and methods

Imaging setup

Our RP-CARS setup is schematically shown in Figure 1 (left). The 810 nm pump-and-probe beam is generated by a Ti-Sa pulsed laser ('fs Laser', Chameleon Vision 2, Coherent Inc., Santa Clara, California, U.S.A.). Part of this beam is used to pump an Optical Parametric Oscillator ('OPO'; Oria IR, Radiantis, Barcelona, Spain) and the 1060-nm signal beam generated by the OPO is used as the Stokes beam (the idler beam of the OPO is dumped). The Ti–Sa laser is optically isolated from the OPO by a Faraday isolator ('Is'), in order to prevent back-reflections from the OPO entering the laser cavity. Each beam passes through an SF6 optical-glass block (G and G′) and a telescopic beam expanders (BE and BE′). The thicknesses of the optical glass blocks were carefully chosen in order to achieve spectral focusing (Rocha-Mendoza *et al.*, 2008) in the sample optical plane by optimal tuning of the pulses group delay dispersion. Before being recombined by means of a 900-nm long-pass dichroic mirror ('D') the Stokes beam is delayed by a delay line ('DL') in order to be temporally overlapped with the pump-and-probe beam and each beam passes through a pair of waveplates. Specifically, the Stokes beam is circularly polarised by means of a pair of λ/4 retarders ('λ/4') that also compensates for polarisation distortions induced by the downstream DMs; whereas a mechanically rotating λ/2 retarder ('R-λ/2') is used in order to continuously rotate the polarisation plane orientation of the linearly polarised pump-and-probe beam and a second fixed λ/4 retarder ('λ/4') on the pump-and-probe beam line is used for the polarisation distortions compensation. The combined pump-and-probe and Stokes beams are then routed to the high-numerical-aperture (NA) lens ('Obj', Objective C-Achroplan W, 32X, NA = 0.85, Carl Zeiss MicroImaging GmbH, Göttingen, Germany) of an inverted microscope (Axio Observer Z1, Carl Zeiss MicroImaging GmbH, Göttingen, Germany) through a pair of galvo-scanning mirrors ('XY', GVS002, Thorlabs, Newton, New Jersey, U.S.A.), a scan lens, a dichroic mirror, a compensation lens, and a tube lens. This lens arrangement is further described in the 'Results and discussion' section of this paper. The CARS signal originated from the sample ('S') is collected both in the trans-direction by a condenser lens ('Cond', NA = 0.55) and in the epi-direction and then detected by means of red-sensitive photomultiplier tubes ('PMT', R3896, Hamamatsu, Hamamatsu City, Japan). In the trans-direction the CARS signal is edge-filtered to remove the pump photons and band-pass filtered (BP, filter centred at 650 nm and with a full width at half maximum of 50 nm) to select the Raman band of the CH_2 bonds (2850 cm^{-1}). In the epi-direction the CARS signal is routed to the detector by means of a dichroic mirror (‘D’) situated between the compensation lens and the scan lens and then filtered in the same way as the trans-direction signal (‘BP’) and focalised by an additional lens. Silver-coated mirrors are labelled with ‘M’. The output of the photomultiplier tubes and the signal generated by the Hall sensor of the brushless motor that rotates the $\lambda/2$ waveplate are acquired by a digital acquisition board (‘Software Lock-in’, USB-6366, National Instruments Corporation, Austin, Texas, U.S.A.) and elaborated by a custom-made software (written in LabVIEW programming language, Lab-VIEW 2010 SP1, National Instruments Corporation, Austin, Texas, U.S.A.) running on a PC to compute – in real time and for each pixel – the dc component (A_{dc}), $A_{2\omega,}$ and Φ of the raw CARS signal. This acquisition method was described in great details in de Vito & Piazza (2014).

Biological sample preparation and observation

Unfixed spinal cord of a 23-month-old wild-type mouse (C57BL/6 strain, Harlan Italy, Correzzana, Italy) was used. The spinal cord was frozen at −80 °C immediately after the explant and kept at this temperature until the observation.

The thawed tissue was put in the central well of a Krebs–Henseleit Buffer (K3753 Sigma-Aldrich, St. Louis, Missouri, U.S.A.) filled WillCo dish (GWSt-3512, WillCo Wells, Amsterdam, the Netherlands) and kept immobilised with a glass coverslip glued to the lateral polystyrene support of the dish. The tissue was finally imaged in epi-direction through the thin (0.17 mm) glass bottom of the dish central well.

Results and discussion

The optical setup presented in this paper is specifically optimised to obtain high acquisition rates and to retain at the same time a sufficient SNR for polarisation-resolved CARS imaging (RP-CARS). For this purpose, we have dedicated particular attention to several technical aspects: the generation of the incoming beams, the spectral focusing, the movements of the scanning mirrors, the minimisation of the polarisations distortions and the optimisation of the acquisition process.

In the setup described in this paper, we have used an OPO in order to generate the Stokes beam and exploited the principle of spectral focusing (Hellerer *et al.*, 2004) by dispersing the Stokes and pump beams with glass blocks of carefully calculated lengths (Rocha-Mendoza *et al.*, 2008). The thickness of the optical glasses is computed in order to yield approximately 20,000 fs^2 of GDD at the wavelengths here of interest for both the beams (Ciofani *et al.*, 2014). The acquisition process consists, as described in de Vito & Piazza (2014), in repeatedly scanning a line of the image with one galvanometric mirror, while at the same time rotating the retarder (we used a rotation frequency of 10 Hz for all the images in this article). During the acquisition of the next line, a software algorithm reconstructs the temporal evolution of the CARS signal for each pixel and performs a lock-in-like phase-detection algorithm. This approach requires moving the galvanometric mirrors at high speed to allow collecting the signal from an entire line multiple times within each rotation of the polarisation plane, potentially causing imaging artefacts – images look ‘smeared’ at the border – at the two ends of each scanning line, where the fast-scanning mirror has to decelerate and then accelerate in the new scanning direction. In order to reduce these artefacts we perform the acquisition only in one motion direction, where the mirror position is set to change linearly with time, at constant velocity (v_0), and used a fourth-degree polynomial to describe the mirror set-position $x(t)$ versus time during the return phase:

$$x(t) = a \times t^4 + b \times t^3 + c \times t^2 + d \times t + e. \tag{1}$$

For the set-position function to be as smooth as possible (thereby minimizing the set/real position mismatch), we have imposed the following conditions: the function continuity at the extremities, $x(t_0) = x_0$; $x(-t_0) = -x_0$, the velocity continuity at the end of the return phase, $\dot{x}(t_0) = v_0 = \frac{x_0}{t_0}$, zero acceleration at the end of the return phase, $\ddot{x}(t_0) = 0$ and zero velocity at the central temporal point of the return phase $\dot{x}(0) = 0$.

With those constrains, $x(t)$ becomes

$$x(t) = -\frac{x_0}{4 \times t_0^4} \times t^4 + \frac{x_0}{t_0^3} \times t^3 - \frac{3 \times x_0}{2 \times t_0^2} \times t^2 + \frac{7 \times x_0}{4}, \tag{2}$$

where $2 \times x_0$ is the total deflection and $2 \times t_0$ the time needed for the mirror to cover it.

This approach successfully suppresses the smearing artefacts while keeping overall a high scan speed, albeit changing the acquisition speed still produces a small but measurable spatial shift of the images, caused by the lag in the mirror real position versus set one.

As noted above, the DMs are the major cause of polarisation distortions and this is particularly true when the light incidence angle on those mirrors varies during the scan. The DM used to collect the signal in epi-direction must be positioned as close as possible to the objective, in order to maximise the collection efficiency. Conveniently, the DM may be placed between the tube lens and the scans lens. An additional lens mounted between the DM and the PMT images the objective pupil onto the PMT surface. If the objective rear aperture is in the focal plane of the tube lens, then it would be possible to implement a 4-f configuration by placing the scan lens so that its focal plane and that of the tube lens coincide. In this case the incoming beam axis would always be parallel with respect to the optical axis in the segment between the scan lens and the tube lens, irrespective of the position of the galvanometric mirrors. Therefore, its angle of incidence with respect to the

DM would be always constant. However, if the objective rear aperture is not in the focal plane of the tube lens, as in the case of ours and other commercial microscopes, then it is not possible to achieve this ideal situation. However, we show that this problem can be overcome by placing a compensation lens between the DM and the tube lens, as displayed in Figure 1 (right), and positioning the scan lens at a focal-length distance from the galvanometric mirrors. In this way the incoming-beam axis remains always parallel with respect to the optical axis in the region between the two lenses and therefore through the DM, independently from the galvanometric-mirror positions. In order for the beam to be collimated in the objective rear aperture, the distance between the compensation lens and the tube lens ($h\prime$) and the distance (h) between the scan lens and the compensation lens are adjusted so that the focal plane of the virtual lens constituted by latter two coincides with the focal plane of the tube lens.

$$f_t + BFL_{s,c} = h', \tag{3}$$

where $BFL_{s,c} \equiv (f_s - h) \times f_c/(f_s + f_c - h)$ is the back focal length of this virtual lens, and f_s, f_c, f_t are the focal lengths of the scan, compensation, and tube lenses, respectively. Finally, in order to have constant illumination of the pupil throughout the scanning range the set of the three lenses has to image the scan mirrors onto the pupil of the objective, or – equivalently – the latter has to be placed on the focal plane of the virtual lens composed by the compensation and tube lenses:

$$BFL_{c,t} \equiv (f_c - h') \times f_t/(f_c + f_t - h') = d, \tag{4}$$

where d is the distance between the objective rear aperture and the tube lens. Equations (3) and (4) show that, for a given scan lens and tube lens, several combinations of f_c, h' and h can be used, conveniently allowing to select the compensating lens from available stock lenses and determining h and $h\prime$consequently.

In our microscope the scan lens was constituted of a pair of achromatic lenses (AC254–200-B and AC254–150-B, with focal lengths of 20 and 15 cm, respectively, Thorlabs, Newton, New Jersey, U.S.A.), selected by means of simulations with Oslo 66 to yield minimum aberrations. The lenses are placed with their most convex optical surfaces facing each other, with the 20-cm lens mounted closer to the mirrors. The effective focal length of this combination was calculated to be approximately 9.0 cm. In our microscope, we had: $f_t = 16.5$ cm, $d = 12$ cm. Selecting a compensation lens with a focal length of 60 cm, yielded: $h = 9.5$ cm and $h' = 16$ cm. Final adjustments to the lens positions in the real setup were performed by maximising the field-of-view while keeping the CARS imaging plane coincident with the naked-eye-observation plane.

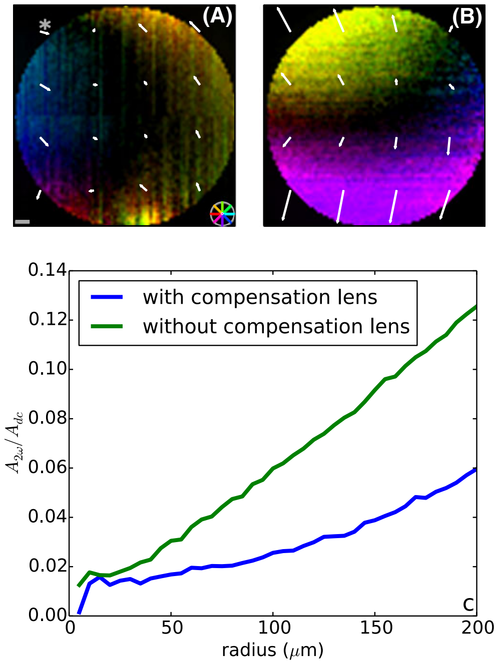

Fig. 2. (A) and (B) Nonresonant RP-CARS images (2850 cm^{-1}) of the glass bottom of a WillCo-dish plate taken with (A) and without (B) the compensation lens. The images were built in the HSV ('hue', 'saturation', 'value') colour space, mapping the Φ values onto the 'hue' channel (as shown in the colour wheel in the bottom right corner of (A) and mapping the ratio between $A_{2\omega}$ and A_{dc} onto the 'value' channel, while keeping the saturation channel values at maximum. The average local hue is indicated by the direction of the white arrows, whereas the average local value is indicated by their length. Scale bar: 25 microns. The length of the arrow labelled with * corresponds to a ratio $A_{2\omega}/A_{\mathrm{dc}}$ equals to 0.04. Acquisition time: 6 minutes for 100 × 100 pixels. (C) Plot of the ratio $A_{2\omega}/A_{\mathrm{dc}}$ averaged over a circumference as a function of the radius of the latter. The circumference is centred in the middle of the scan area.

To validate this approach we quantified the residual polarisation distortions in our setup by acquiring a nonresonant large-scale RP-CARS image of a glass slide. Since the glass is isotropic and amorphous in an ideal condition the $A_{2\omega}$ signal would be zero. Therefore, in real conditions, the ratio $A_{2\omega}/A_{\mathrm{dc}}$ is a measure of the residual polarisation distortions and the phase indicates the spatial orientations of the induced distortions. As displayed in Figure 2, the magnitude of the distortions increases with the distance from the centre of the image. Nevertheless, its maximum – approximately 6%, observed at the periphery of the large-scale image – is negligible (approximately five times smaller) with respect to the anisotropy values usually detected from the biological samples (e.g. myelin sheaths of mouse nerves) with similar approaches (de Vito *et al.*, 2014). Without the compensation lens, it is still possible to compensate for the polarisation distortions in the centre of the image field but those distortions are consistently bigger than the first case over the whole area of the image field (Fig. 2C) and they increase up to 12.8% in the image periphery, as displayed in Figure 2B.

Finally, we report an RP-CARS large-scale (0.5 mm × 0.5 mm) image of a pair of mouse nerve rootlets at their point of emergence from the spinal cord. The field of interest was identified using bright-field microscopy (Fig. 3A) and then

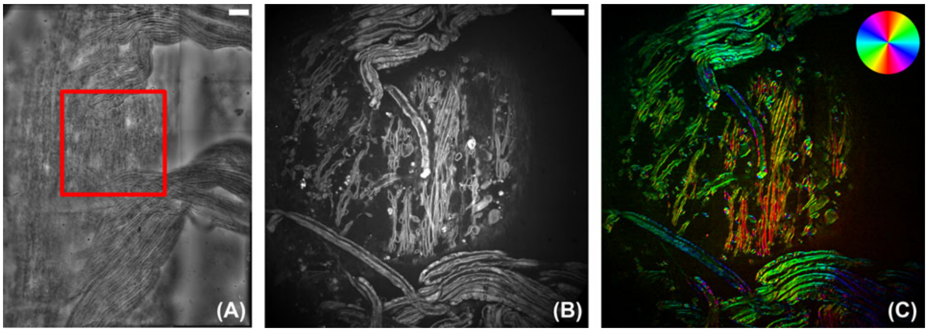

Fig. 3. Large-scale RP-CARS image (2850 cm^{-1}, CH_2 bonds) of a couple of mouse nerve rootlets at their point of emergence from the spinal cord. (A) Bright-field image. Scale bar: 100 μm. The image is a mosaic, made by stitching 3 × 3 tiles acquired by moving the sample stage. (B) RP-CARS image of the region in red square in (A), created by mapping A_{dc} to grey-values. Scale bar: 50 μm. (C) RP-CARS image of the same region as in (B). This image was created in the HSV colour space, mapping the Φ values onto the 'hue' channel (as shown in the colour circle in the top right corner of the panel) and mapping $A_{2\omega}$ onto the 'value' channel, while keeping the saturation channel values at maximum. (B) and (C) are mosaics, made by automatic stitching 3 × 3 tiles acquired by scanning different field region with the galvanometric mirrors. Total acquisition time for CARS images: 47 minutes for overall 556 × 556 pixels.

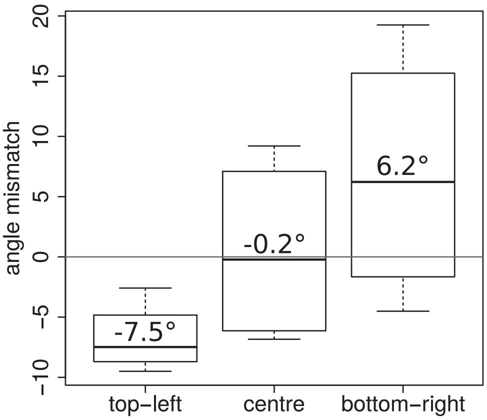

Fig. 4. Box plot of the difference between the Φ values of the CH_2 bonds inside the myelin walls and the spatial orientation angles of the respective myelin walls in diverse areas of the image field depicted in Figure 3. The blue line shows the zero difference point, that is, where the data would lay in absence of polarisation distortions. The median values of the differences are reported on the respective bars.

imaged by RP-CARS to visualize the CH_2-rich myelin of the nervous fibres (Fig. 3B). The measured average spatial orientation of the CH_2 bonds inside the PSF is shown in (Fig. 3C). In order to verify if the polarisation-based information is correctly retrieved even in the peripheral parts of this large-scale image, we compared the spatial orientation of individual myelin walls with their average Φ value. Since most of the CH_2 bonds inside myelin are orientated parallel with respect to the wall surface, in the absence of polarisation distortions the average Φ value corresponds to the myelin wall orientation. Figure 4 demonstrates that the average Φ value coincides within the experimental errors with the spatial orientation of the fibre in the centre of the image (where the polarisation distortions were minimised by adjusting the compensating retarders) and that they are extremely consistent (the average mismatch is less than 7 degrees) even in the far peripheral areas of this large-field image, where the polarisation distortions are the largest.

Although the use of a high-NA objective leads to the generation of polarisation components along the optical axis, this has a negligible effect on the orientation detection, because it does not induce a deformation of the polarisation response (Schön *et al.*, 2008). Moreover, for objectives with NA = 0.85, such as the one used in the present work, the polarisation component along the optical axis is less than 10% of the transversal component (Kang *et al.*, 2010) and is therefore possible to neglect its effects.

It should be noted that PR laser-scanning microscopy can be performed also by scanning the sample and keeping the incoming rays fixed in space. If on the one hand this configuration is very effective in minimizing the polarisation distortions all over the field-of-view, on the other the acquisition is typically very slow because it requires moving the microscope stage. On the contrary, the methods presented in this article, making use of the galvanometric mirrors, allow for fast laser-scanning PR imaging of large-spatial-scale quick phenomena, opening up new possibilities for the applications of this microscopy. An example is given in a recent article (de Vito *et al.*, 2014), where a relatively fast (approximately 45 minutes) chemically induced demyelination process is observed in high temporal (40 seconds per frame) and spatial (pixel size: 0.5 micron) resolution with RP-CARS without significant polarisation distortions in the field-of-view (50 micron × 50 micron).

Moreover, the preservation of the polarisation characteristics of the incident beams all over the field can be useful also in other CARS implementations, for example, P-CARS, where linearly polarised pump-and-probe and Stokes beams at different angles, and polarised detection, are used in order to suppress the nonresonant background (Cheng *et al.*, 2001).

Conclusions

Polarisation-resolved laser scanning microscopy encompasses a set of powerful imaging techniques able to detect structural information of the sample under investigation – for example, the average orientation of CH_2 bonds – inside the focal volume. One of the most important limiting factors of these imaging techniques is the size of the field-of-view, restricted from the polarisation distortions induced by the optical elements for sufficiently high scanning angles.

In this paper we discussed a practical approach able to optimize the RP-CARS imaging and particularly to maximise its field-of-view and we quantify the amount of residual distortions. While focused on CARS imaging, the approach described here can be successfully exploited in a wide range of other PR laser scanning imaging techniques.

References

Bélanger, E., Bégin, S., Laffray, S., De Koninck, Y., Vallée, R. & Côté, D. (2009) Quantitative myelin imaging with coherent anti-Stokes Raman scattering microscopy: alleviating the excitation polarization dependence with circularly polarized laser beams. *Opt. Exp.* **17**, 18419–18432.

Bélanger, E., Turcotte, R., Daradich, A., Sadetsky, G., Gravel, P., Bachand, K., De Koninck, Y. & Côté, D. (2015) Maintaining polarization in polarimetric multiphoton microscopy. *J. Biophot.* DOI: 10.1002/jbio.201400116.

Bioud, F.-Z., Gasecka, P., Ferrand, P., Rigneault, H., Duboisset, J. & Brasselet, S. (2014) Structure of molecular packing probed by polarization-resolved nonlinear four-wave mixing and coherent anti-Stokes Raman-scattering microscopy. *Phys. Rev. A* **89**, 013836-01–013836-10.

Cheng, J. X., Book, L. D. & Xie, X. S. (2001) Polarization coherent anti-Stokes Raman scattering microscopy. *Opt. Lett.* **26**, 1341–1343.

Ciofani, G., Del Turco, S., Rocca, A. et al. (2014) Cytocompatibility evaluation of gum Arabic-coated ultra-pure boron nitride nanotubes on human cells. *Nanomedicine* **9**, 773–788.

de Vito, G. & Piazza, V. (2014) Fast signal analysis in rotating-polarization CARS microscopy. *Opt. Data Process. Storage* **1**, 1–5.

de Vito, G., Bifone, A. & Piazza, V. (2012) Rotating-polarization CARS microscopy: combining chemical and molecular orientation sensitivity. *Opt. Exp.* **20**, 29369–29377.

de Vito, G., Tonazzini, I., Cecchini, M. & Piazza, V. (2014) RP-CARS: label-free optical readout of the myelin intrinsic healthiness. *Opt. Exp.* **22**, 13733–13743.

Duboisset, J., Aït-Belkacem, D., Roche, M., Rigneault, H. & Brasselet, S. (2012) Generic model of the molecular orientational distribution probed by polarization-resolved second-harmonic generation. *Phys. Rev. A* **85**, 043829-01–043829-9.

Ferrand, P., Gasecka, P., Kress, A., Wang, X., Bioud, F.-Z., Duboisset, J. & Brasselet, S. (2014) Ultimate use of two-photon fluorescence microscopy to map orientational behavior of fluorophores. *Biophys. J.* **106**, 2330–2339.

Finzi, L. & Bustamante, C.J. (1988) Design and application of a computer-controlled confocal scanning differential polarization microscope. *Rev. Sci. Instr.* **59**, 2399–2408.

Gasecka, A., Han, T. J., Favard, C., Cho, B. R. & Brasselet, S. (2009) quantitative imaging of molecular order in lipid membranes using two-photon fluorescence polarimetry. *Biophys. J.* **97**, 2854–2862.

Gupta, V. K. & Kornfield, J. A. (1994) Polarization modulation laser scanning microscopy: a powerful tool to image molecular orientation and order. *Rev. Sci. Instr.* **65**, 2823–2828.

Gusachenko, I., Latour, G. & Schanne-Klein, M.-C. (2010) Polarization-resolved second harmonic microscopy in anisotropic thick tissues. *Opt. Exp.* **18**, 19339–19352.

Hellerer, T., Enejder, A. M. K. & Zumbusch, A. (2004) Spectral focusing: High spectral resolution spectroscopy with broad-bandwidth laser pulses. *Appl. Phys. Lett.* **85**, 25–27.

Kang, H., Jia, B. & Gu, M. (2010) Polarization characterization in the focal volume of high numerical aperture objectives. *Opt. Exp.* **18**, 10813–10821.

Kress, A., Wang, X., Ranchon, H., Savatier, J., Rigneault, H., Ferrand, P. & Brasselet, S. (2013) Mapping the local organization of cell membranes using excitation-polarization-resolved confocal fluorescence microscopy. *Biophys. J.* **105**, 127–136.

Maker, P. D. & Terhune, R. W. (1965) Study of optical effects due to an induced polarization third order in the electric field strength. *Phys. Rev.* **137**, A801–A818.

Mazumder, N., Qiu, J., Foreman, M. R., Romero, C. M., Hu, C.W., Tsai, H. R., Török, P. & Kao, F. J. (2012) Polarization-resolved second harmonic generation microscopy with a four-channel Stokes-polarimeter. *Opt. Exp.* **20**, 14090–14099.

Munhoz, F., Rigneault, H. & Brasselet, S. (2012) Polarization-resolved four-wave mixing microscopy for structural imaging in thick tissues. *J. Opt. Soc. Am. B* **29**, 1541–1550.

Plotnikov, S.V., Millard, A.C., Campagnola, P.J. & Mohler, W.A. (2006) Characterization of the myosin-based source for second-harmonic generation from muscle sarcomeres. *Biophys. J.* **90**, 693–703.

Rocha-Mendoza, I., Langbein, W. & Borri, P. (2008) Coherent anti-Stokes Raman microspectroscopy using spectral focusing with glass dispersion. *Appl. Phys. Lett.* **93**, 201103-1–201103-3.

Savoini, M., Wu, X., Celebrano, M. *et al.* (2012) Circular dichroism probed by two-photon fluorescence microscopy in enantiopure chiral polyfluorene thin films. *J. Am. Chem. Soc.* **134**, 5832–5835.

Schön, P., Munhoz, F., Gasecka, A., Brustlein, S. & Brasselet, S. (2008) Polarization distortion effects in polarimetric two-photon microscopy. *Opt. Exp.* **16**, 20891–20901.

Steinbach, G., Pomozi, I., Zsiros, O., Menczel, L. & Garab, G. (2009) Imaging anisotropy using differential polarization laser scanning confocal microscopy. *Acta Histochemica* **111**, 317–326.

Tiaho, F., Recher, G. & Rouède, D. (2007) Estimation of helical angles of myosin and collagen by second harmonic generation imaging microscopy. *Opt. Exp.* **15**, 12286–12295.

Zimmerley, M., Younger, R., Valenton, T., Oertel, D.C., Ward, J.L. & Potma, E.O. (2010) Molecular orientation in dry and hydrated cellulose fibers: a coherent anti-stokes raman scattering microscopy study. *J. Phys. Chem. B* **114**, 10200–10208.